

Model for transitional turbulence in a planar shear flow

Santiago J. Benavides and Dwight Barkley

Mathematics Institute, University of Warwick,

Coventry CV4 7AL, United Kingdom

(Dated: September 4, 2023)

Abstract

A central challenge to understanding the route to turbulence in wall-bounded flows is that the flows are composed of complex, highly fluctuating, and strongly nonlinear states. We address this challenge by deriving from the Navier-Stokes equations a simplified model that describes transitional turbulence in a planar setting. The Reynolds-averaged and turbulent-kinetic-energy equations are projected onto a minimal set of wall-normal modes and justified model closures are used for the Reynolds stresses and turbulent dissipation and transport. The model reproduces the oblique turbulent-laminar patterns ubiquitous in wall-bounded shear flows. The model captures the pattern wavelengths and angles, and the large-scale flow associated with both stationary patterns and growing turbulent spots. Patterns are shown to arise with decreasing Reynolds number via a linear instability of uniform turbulence. Linear analysis reveals implications for the critical angle at onset.

The route to turbulence in many wall-bounded shear flows is mediated by a fascinating regime in which turbulence cannot be sustained throughout the system; rather it occurs intermittently within laminar flow [1–4]. While the laminar state is stable to small perturbations, strongly nonlinear patches of turbulence may be sustained via interactions with the neighboring quiescent laminar flow [5–8]. Turbulent patches exhibit growth, splitting and decay, with each process occurring at different rates depending on system control parameters. One of the more intriguing and pervasive manifestations of intermittent turbulence is the alternation of regions of turbulent and laminar flow oriented obliquely to the streamwise direction [3, 9–23]. Figure 1 illustrates a large-scale pattern formed by such alternation in the planar shear flow described fully below. The scale of these patterns is more than an order of magnitude larger than the constrained direction of mean shear – the scale at which the turbulence is generated [9–11, 14, 17]. Observations of oblique turbulent structures (often now called turbulent bands or stripes) trace back to the observations of spiral turbulence between counter rotating cylinders [24], and have been the subject of much study ever since [3].

The boundaries of the intermittent turbulence regime are of particular interest. With decreasing flow rate, or Reynolds number (Re), turbulent bands take a localized and fragmented form, and eventually a critical point is reached below which turbulence is not sustained. Universal scaling laws associated with directed percolation (DP) have been estab-

lished for such critical points in some flows [21, 25–27]. With increasing Re , laminar regions disappear and bands give way to a uniform turbulent state whose mean recovers the full symmetry of the flow geometry. Equivalently, a symmetry breaking of the uniform turbulent state occurs with decrease Re . A substantial body of previous work has analysed and characterized the transition from uniform turbulence [8, 9, 16, 23, 28–30]. Most recently, Kashyap *et al.* provide strong evidence for a linear instability of the uniform turbulent state by considering the ensemble-averaged relaxation rates to perturbations [23], while Gomé *et al.* [8, 30] analyze the energy balances and fluctuations associated with this transition.

Models provide a powerful means to investigate the complex transition scenarios exhibited by wall-bounded turbulence and several distinct approaches have been proposed [29, 31–38]. The most relevant here is the modeling of pipe flow [33–35] by two scalar fields: the amplitudes of large-scale (coarse-grained) turbulence and mean flow. The amplitudes depend only on the axial coordinate and are governed by advection-reaction-diffusion equations modeling the interaction between the mean flow and turbulence, with the effect of “microscopic” turbulent fluctuations accounted for with an additional noise term. This modeling does not readily extend to the planar case, however, primarily because the large-scale flow in the planar case must be described by a vector field. Fluid advection plays a significant role in these flows [6, 8, 17] and the vector nature of mean flow must be appropriately accounted for in modeling. In this Letter we derive a quantitative model of planar shear turbulence directly from the Navier-Stokes equations through specified truncations and model closures.

We start our derivation from the most mathematically tractable system exhibiting turbulent-laminar bands: a shear layer confined between stress-free boundaries, driven by a sinusoidal body force. In the transition literature, the system is called Waleffe Flow (WF), after Waleffe who used it in his work on the self-sustaining process [39]. Waleffe flow reproduces the same transitional phenomena as plane Couette flow (pCf) [3, 18], and has been used to access very large system sizes [26].

In the spirit of previous pipe models, we describe the dynamics of the large-scale (coarse-grained) variables. We apply Reynolds averaging to the Navier-Stokes equations and denote the mean (or ‘large-scale’) velocity by \mathbf{u} and the fluctuations by \mathbf{u}' , where $\langle \mathbf{u}' \rangle = 0$ with $\langle \cdot \rangle$ is a suitable averaging procedure. We define the turbulent kinetic energy (TKE) as $q \equiv \langle \mathbf{u}' \cdot \mathbf{u}' \rangle / 2$. In practice, one averages over intermediate spatial-temporal scales that are long on the scale of the turbulence but short on the scale of the patterns. Averaging has the

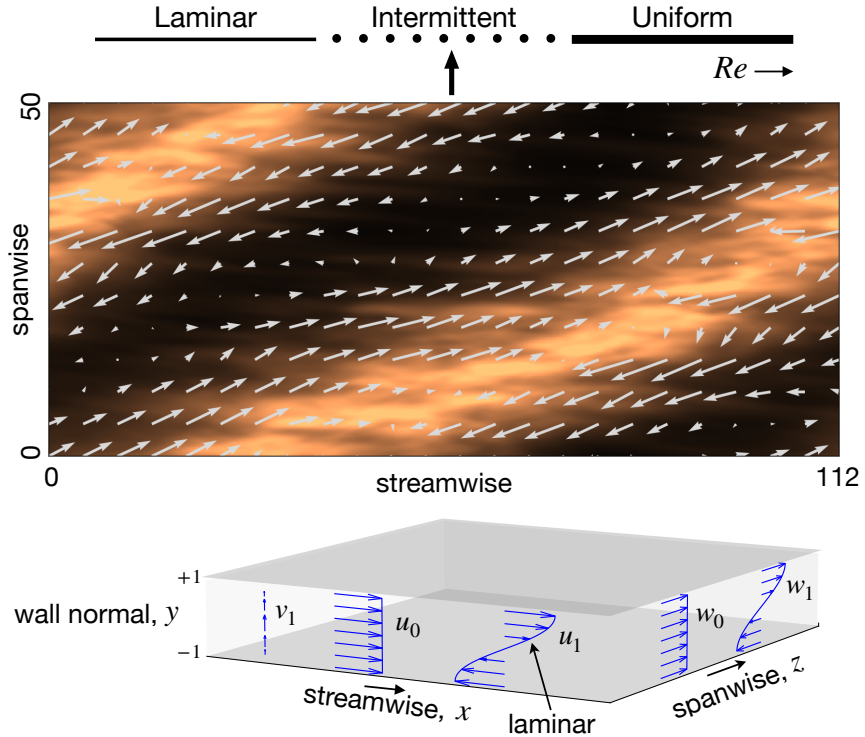


FIG. 1. (a) Illustration of oblique turbulent-laminar patterns in a planar shear flow confined by stress-free walls and driven by a body-force. These states are observed in the intermittent regime where turbulence can exist, but is not uniform (space filling). Visualized in color is the time- and vertically-averaged turbulent kinetic energy (TKE) from a direct numerical simulation at $Re = 140$ in a streamwise-spanwise periodic domain. The arrows correspond to the time- and vertically-averaged velocity field. The averages were taken over a window of 280 advective time units. (b) Flow geometry, with illustrations of the five wall-normal (vertical) modes in the model used to represent the large-scale flow. One of these modes is the same laminar flow: $\sin(\pi y/2)\mathbf{e}_x$. Horizontal dimensions of interest, as in (a), are vastly larger than depicted in (b).

effect of removing small turbulent scales, and while \mathbf{u} is formally defined as a mean, we view it as a large-scale flow. Our coordinates (x, y, z) correspond to the streamwise, wall-normal, and spanwise directions, respectively. The components of the large-scale velocity \mathbf{u} are denoted by (u, v, w) . We non-dimensionalize using the vertical half gap h and the maximum laminar velocity U , resulting in a domain of dimensions $L_x \times 2 \times L_z$, with $y \in (-1, 1)$. We use $\beta \equiv \pi/2$ for the first vertical wavenumber.

After Reynolds averaging one obtains [40],

$$\frac{\partial \mathbf{u}}{\partial t} + \mathbf{u} \cdot \nabla \mathbf{u} = -\nabla p + \frac{1}{Re} \nabla^2 \mathbf{u} - \alpha \mathbf{u}_H + \mathbf{F} + \nabla \cdot \mathcal{R}, \quad (1a)$$

$$\frac{\partial q}{\partial t} + \mathbf{u} \cdot \nabla q + \nabla \cdot \mathbf{T} = \mathcal{P} - \varepsilon + \frac{1}{Re} \nabla^2 q - 2\alpha q, \quad (1b)$$

where p is the pressure, $Re \equiv Uh/\nu$ is the Reynolds number, ν is the kinematic viscosity, $\mathbf{F} \equiv (\alpha + \beta^2/Re) \sin(\beta y) \mathbf{e}_x$ is the body force which supports a linearly stable laminar flow $\mathbf{u}_{lam} = \sin(\beta y) \mathbf{e}_x$, and α is the drag coefficient. The drag term only acts on the horizontal velocity components $\mathbf{u}_H \equiv u \mathbf{e}_x + w \mathbf{e}_z$ to mimic the effect of no-slip boundaries [3, 41], and is only relevant for y -independent modes and at large horizontal scales. The Reynolds-stress tensor \mathcal{R} , the turbulent production \mathcal{P} , the pseudo-dissipation rate ε , and the transport terms \mathbf{T} , are defined by standard expressions [40]. Each involves fluctuation correlations and closure comes from modeling these quantities. Equations (1) are accompanied by an incompressibility constraint $\nabla \cdot \mathbf{u} = 0$, periodic boundary conditions in the (x, z) directions, and stress-free boundary conditions $\partial_y u = v = \partial_y w = \partial_y q = 0$ at $y = \pm 1$.

We turn to modeling and continue to use variables \mathbf{u} and q . Our first step is to represent \mathbf{u} and q with a minimal set of wall-normal (vertical) modes given by

$$u(x, y, z, t) = u_0(x, z, t) + u_1(x, z, t) \sin(\beta y), \quad (2a)$$

$$v(x, y, z, t) = v_1(x, z, t) \cos(\beta y), \quad (2b)$$

$$w(x, y, z, t) = w_0(x, z, t) + w_1(x, z, t) \sin(\beta y), \quad (2c)$$

$$q(x, y, z, t) = q_0(x, z, t) + q_1(x, z, t) \sin(\beta y), \quad (2d)$$

and pressure $p(x, y, z, t) = p_0(x, z, t) + p_1(x, z, t) \sin(\beta y)$. The retained modes are the minimal set describing a three-dimensional vector field. The field q_1 will be obtained quasi-statically from the other fields, and hence the model is represented in six dynamical fields: $u_0, u_1, v_1, w_0, w_1, q_0$, that are functions of (x, z, t) . Substitution of (2) into (1), followed by a Galerkin projection, gives evolution equations for the six fields.

To complete the model, we need to specify closures for \mathcal{R} , \mathcal{P} , ε , and \mathbf{T} . We seek to express these as functions of q and Re that are as simple as possible consistent with data from direct numerical simulations (DNS) of the Navier-Stokes equations. For the Reynolds stress \mathcal{R} , we let $\mathcal{R}_{12} = \mathcal{R}_{21} = -\langle u'v' \rangle = A(q_0) \cos(\beta y)$, and neglect all other tensor components. We use $A(q_0) = a((q_0^2 + \eta^2)^{1/2} - \eta)$, where a and η parameters with η small. This gives A approximately linear in q_0 , except near $q_0 = 0$ where A becomes approximately quadratic in q_0 . This

cut-off in production at small q_0 is responsible for maintaining stability of model laminar fixed point for all Re . The turbulent production \mathcal{P} is specified from \mathcal{R} and $\nabla \mathbf{u}$, and requires no additional modeling. For the transport term we invoke the gradient-diffusion hypothesis [40] that states $\mathbf{T} = -\nu_T(q_0; Re)\nabla q_0$. DNS suggest that ε and ν_T can be sufficiently well modeled as linear functions of q_0 and we use: $\varepsilon(q_0; Re) = c q_0/Re$ and $\nu_T(q_0; Re) = d Re q_0$, with parameters c and d . Modelling the q_1 dynamics as an instantaneous balance between nonlinear advection and dissipation, q_1 is determined instantaneously from u_1, w_1 , and q_0 .

In summary, the model is represented by six fields, $u_0, u_1, v_1, w_0, w_1, q_0$, corresponding to the mode amplitudes of large-scale flow and TKE. The evolution equations of these dynamical fields in (x, z, t) are obtained by substituting expansion (2) into equations (1), using model closures for $\mathcal{R}, \mathcal{P}, \varepsilon$, and \mathbf{T} , using a quasi-static approximation for q_1 , imposing incompressibility, and applying a Galerkin projection. The six evolution equations are stated in full in the Supplemental Material, together with details on the model derivation and closures [42].

The model possesses spatially uniform steady states of the form $(u_0, u_1, v_1, w_0, w_1, q_0) = (0, u_{ss}, 0, 0, 0, q_{ss})$, where u_{ss} and q_{ss} satisfy the equations for u_1 and q_0 after dropping x, z , and t derivatives [42]. We denote these steady states by (u_{ss}, q_{ss}) . Laminar flow is the steady state $(1, 0)$, existing for all Re . Above $Re = 72.4$, the model also possesses a pair of non-trivial steady states with $u_{ss} < 1$ and $q_{ss} > 0$, corresponding to uniform turbulence. One of these states (the ‘upper state’) is stable to spatially uniform perturbations. Hence, the spatially uniform dynamics is bistable for $Re \geq 72.4$.

We simulate the six model equations on a doubly-periodic domain of size $L_x \times L_z$ using the open source pseudo-spectral code Dedalus [43]. Second-order Runge-Kutta time stepping is used with a time step $\Delta t = 0.04$ (approximately ten times larger than needed in an equivalent DNS). A Fourier-spectral method with 3/2 dealiasing is used with a resolution of one grid point per space unit (approximately ten times fewer than a for a DNS). Two initial conditions (ICs) are used. A localized IC comprises a finite region of turbulence of length 25 and width 14 tilted at 24° to the x direction. The second IC is uniform turbulence $(u_0, u_1, v_1, w_0, w_1, q_0)(x, z, 0) = (0, u_{ss}, 0, 0, 0, q_{ss})$. In all cases, the initial large-scale flow fields are additionally seeded with small-scale noise. To account for turbulent fluctuations on the “microscopic scale”, noise may be further included in simulations. We do not consider this here. The only source of randomness is the ICs. The code and analysis scripts can be

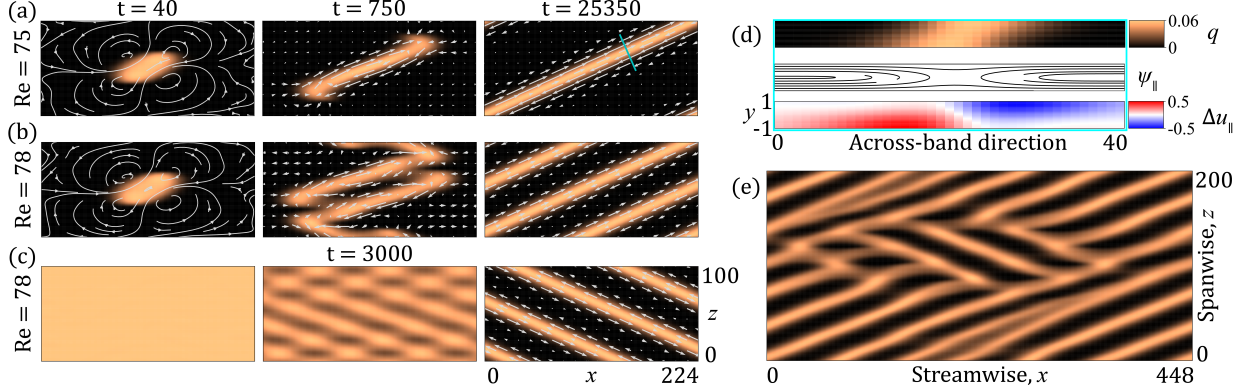


FIG. 2. Temporal evolution of the model for increasing Re , starting from localized (a)-(b), and uniformly turbulent (c) initial conditions. Visualized is the model field q_0 , representing the vertically-averaged turbulent kinetic energy. Vectors and streamlines show the vertically-averaged large scale flow. Panel (d) shows a vertical slice of the reconstructed turbulence field q (top panel) and large scale flow velocities (bottom two panels), taken across the final steady band in (a) (see cyan line). The middle panel in (d) shows the two-dimensional in-plane flow, or equivalently contours of the streamfunction ψ_{\parallel} , whereas the bottom panel shows the along-band flow visualized as a deviation from the laminar flow, $\Delta u_{\parallel} \equiv u_{\parallel} - u_{lam,\parallel}$, where \parallel is the direction parallel to the band. Panel (e) shows an instantaneous snapshot of a run at $Re = 80$ performed in a larger domain than those in panels (a)-(c). Note the two competing band orientation domains.

found in the GitHub repository of the first author [44].

The model results that follow reproduce many published features of bands seen in experiments and DNS. Figure 2(a) shows a simulation at $Re = 75$ starting from the localized ICs. During the initial evolution, the large-scale flow first adjusts to the presence of the turbulent patch, resulting in a large-scale, quadrupolar velocity field. Such fields are well documented [17, 18, 22, 31, 45–49], and reproducing them is an important validation of the model. As the elongated turbulent patch begins to grow, it does so through the growth of its two tips. The two tips eventually join and the system settles into a single steady, straight turbulent band tilted at $\theta = 24^\circ$ to the streamwise direction. The large-scale flow is typical of that observed in experiments and DNS [6, 8, 17, 24, 50]. While the final angle is set in part by the domain, during band elongation (Fig. 2(a), $t = 750$), the tilt angle is not far from $\theta = 24^\circ$.

Figure 2(b) shows a simulation at $Re = 78$. At this slightly higher value of Re we observe

more growth at the tips and also lateral splitting of the band, eventually resulting in two identical steady bands. Figure 2(c) shows the $Re = 78$ case, but starting from the uniform IC. A competition between symmetrically related orientations takes place until eventually a single pair of steady bands emerges. At earlier times, $t = 3000$, the pattern wavelength is approximately $\lambda = 30$, while at the final time $\lambda = 46$. Both lateral splitting [11, 14, 50–52] and band competition [9, 10, 14, 21, 23, 26, 53] are well-documented phenomena.

Figure 2(d) shows a vertical slice of the reconstructed turbulence field q (top panel) and large-scale velocities (bottom two panels), taken across the final steady band at $Re = 75$ (see cyan line in Fig. 2(a), $t = 25350$). The plots are strikingly similar to DNS [3, 6, 8, 18]. The top panel highlights the so-called overhang turbulent regions and demonstrates the role of q_1 in the model. The middle panel visualizes the streamlines of the large-scale flow in the slice plane, while the bottom panel shows contours of the well-documented along-band flow (through the slice plane). The wall-normal structure of the bands seen in Fig. 2(d) highlights that while model fields are functions of (x, z) , they describe nontrivial, three-dimensional flows of the type seen in DNS. The ability to represent such flows is key to the model success.

A survey of the model dynamics reveals the following. The single-band solution can be continued to as low as $Re = 66$, below the onset of bistability in the uniform dynamics. Going upward in Re , beyond $Re = 85$, no bands are observed, and starting from the localized IC, turbulence spreads until a uniformly turbulent steady state (u_{ss}, q_{ss}) is attained. The model dynamics in the range $78 < Re < 85$ is rich. Not all combinations of ICs, Re , and domain size result in simple steady bands. We observe instances of criss-cross-like steady states as well as steady states with both orientations separated by domain boundaries [9, 10], resulting in tilt angles smaller than 24° . In Fig. 2(e) we show a representative snapshot from a simulation that eventually reaches a steady state with two band orientations. Some runs never reach a steady state; bands nearly form, become unstable, break up, and again nearly form to repeat the cycle. (See movies included in the Supplemental Material [42].)

With the model, we can directly address the transition from uniform turbulence to patterns via linear stability analysis. Straightforward linearization of the model equations about (u_{ss}, q_{ss}) gives an eigenvalue problem for the temporal growth rates of linear modes of the form $\hat{\mathbf{u}} \exp(ik_x x + ik_z z)$. (See Supplemental Material [42] for details.) With decreasing Re , a positive real eigenvalue first appears at a critical Reynolds number $Re_c = 85.1$, with a wavelength $\lambda_c = 23.7$ and tilt angle $\theta_c = 22.5^\circ$. Figure 3 shows the maximum growth rates

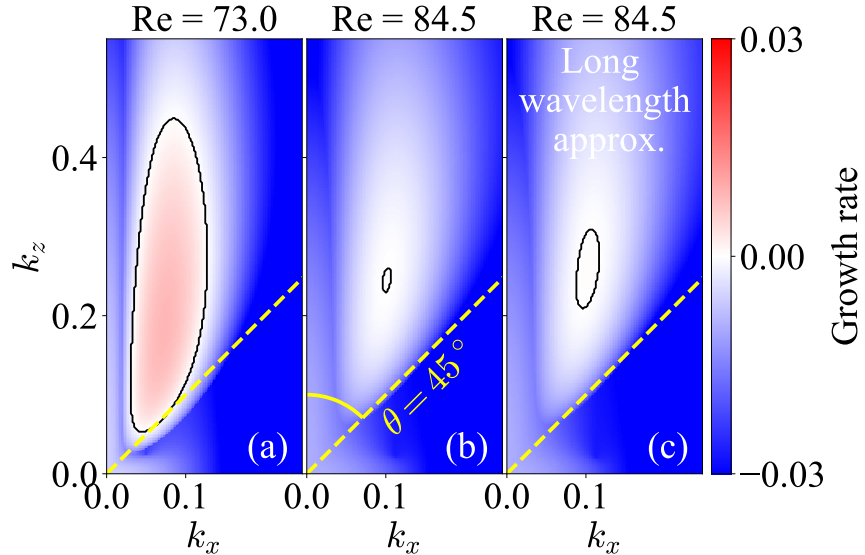


FIG. 3. Maximum growth rate for perturbations of the model equations linearized around the uniformly turbulent state (u_{ss}, q_{ss}) (see text) at a Reynolds number (a) just above the onset of bistability, and (b) just below the critical Reynolds number where a positive growth rate appears. The solid black line represents the neutral stability curve. Panel (c) shows maximum growth rates for perturbations of the simplified linearized equations under the long wavelength assumption ($k \ll \beta$).

in the (k_x, k_z) plane for Re just below Re_c (Fig. 3(b)) and just above the onset of bistability (Fig. 3(a)). With decreasing Re the unstable region enlarges and the fastest growing mode shifts to larger wavelengths and a slightly lower tilt angle ($\lambda \approx 32$ and $\theta \approx 21.5^\circ$ at $Re = 73$). These results align very well with Kashyap *et al.* [23] who extracted evidence of a linear instability of uniform turbulence in plane Poiseuille flow (pPf) and obtained a critical angle of $\theta_c \approx 23^\circ$. Nonlinear model simulations indicate that the bifurcation to bands at Re_c is supercritical.

The model provides a powerful means to explore the mechanisms at work in the formation of bands and in the dynamics of the system. Here we report briefly on one such result: a bound on the selected band angle at onset. (See Supplemental Material [42] for the calculations supporting for the following statements.) Because pattern wavelengths are much larger than the half-gap, i.e. $k \ll \beta$, some terms in the stability equations are small and can be dropped without significantly altering eigenvalues or the nature of the instability. Figure 3(c) shows maximum growth rates for the approximate system. Its critical values are

$\tilde{Re}_c = 87.3$, $\tilde{\lambda}_c = 22.4$ and $\tilde{\theta}_c = 22.0^\circ$. The conditions for a critical zero eigenvalue can be written down and, while they are too complex to fully solve analytically, they can be used to show that the band tilt angle at onset must obey $\tilde{\theta}_c < 45^\circ$ (as highlighted in Fig. 3). Remarkably, this result only requires the stability of the uniform turbulent state to spatially uniform perturbations and is independent of form of the closures. It is possible to improve the bound considerably by exploiting the specific closures used in the model, but we leave this for future work.

In conclusion, we have obtained a quantitatively accurate model of planar shear turbulence from the Navier-Stokes equations, we have shown how it reproduces many known features of transitional turbulence, and we have provided new insights into origins of oblique turbulent bands. Key to the model’s success is its ability to capture the large-scale flows associated with turbulent structures. The model notably retains the non-locality of the Navier-Stokes equations via incompressibility of the large-scale flow. The turbulence closures are natural and simple.

The linear instability of the spatially uniform steady state and the existence of bands are extremely robust to changes in closure parameters. However, the full nonlinear dynamics of the model are more sensitive. In particular, for some parameter values we find instabilities along the bands, as well as instances where the large-scale flow’s amplitude is large, resulting in unrealistic chaotic dynamics. This has restricted parameter values and ultimately resulted in using larger drag, larger α , for the u_0 and w_0 fields. [42].

The model opens several new avenues of research. As has been done for pipe flow [35, 54, 55], a detailed understanding of the transition scenario can be obtained using dynamical systems and bifurcation theory. This could bring new insights into how turbulence is triggered. The small set of physical mechanisms in the model can be exploited to understand how energy balances adjust and ultimately break down with decreasing Re , and this could lead to physical insights into the selection of particular states [8, 30]. One could add new mechanisms to the model or modify the model to describe other flow configurations. Finally, the effect of turbulent fluctuations can be included and the model can be used to investigate rare events [56–58] and percolation transitions [21, 26, 27] in the planar setting.

ACKNOWLEDGMENTS

We wish to thank Sébastien Gomé and Laurette Tuckerman for valuable discussions. This work was supported by a grant from the Simons Foundation (grant no. 662985).

- [1] P. Manneville, European Journal of Mechanics-B/Fluids **49**, 345 (2015).
- [2] P. Mannevill, Mechanical Engineering Reviews **3**, 15 (2016).
- [3] L. S. Tuckerman, M. Chantry, and D. Barkley, Annu. Rev. Fluid Mech. **52**, 343 (2020).
- [4] M. Avila, D. Barkley, and B. Hof, Annu. Rev. Fluid Mech. **55**, 575 (2023).
- [5] I. J. Wygnanski and F. Champagne, J. Fluid Mech. **59**, 281 (1973).
- [6] D. Barkley and L. S. Tuckerman, J. Fluid Mech. **576**, 109 (2007).
- [7] B. Song, D. Barkley, B. Hof, and M. Avila, J. Fluid Mech. **813**, 1045 (2017).
- [8] S. Gomé, L. S. Tuckerman, and D. Barkley, J. Fluid Mech. **964**, A16 (2023).
- [9] A. Prigent, G. Grégoire, H. Chaté, O. Dauchot, and W. van Saarloos, Phys. Rev. Lett. **89**, 014501 (2002).
- [10] A. Prigent, G. Grégoire, H. Chaté, and O. Dauchot, Physica D **174**, 100 (2003).
- [11] D. Barkley and L. S. Tuckerman, Phys. Rev. Lett. **94**, 014502 (2005).
- [12] T. Tsukahara, Y. Seki, H. Kawamura, and D. Tochio, in *Proc. 4th Int. Symp. on Turbulence and Shear Flow Phenomena* (2005) pp. 935–940, arXiv:1406.0248.
- [13] A. Meseguer, F. Mellibovsky, M. Avila, and F. Marques, Phys. Rev. E **80**, 046315 (2009).
- [14] Y. Duguet, P. Schlatter, and D. S. Henningson, J. Fluid Mech. **650**, 119 (2010).
- [15] S. Dong and X. Zheng, J. Fluid Mech. **668**, 150 (2011).
- [16] J. Philip and P. Manneville, Physical Review E **83**, 036308 (2011).
- [17] Y. Duguet and P. Schlatter, Phys. Rev. Lett. **110**, 034502 (2013).
- [18] M. Chantry, L. S. Tuckerman, and D. Barkley, J. Fluid Mech. **791**, R8 (2016).
- [19] M. Shimizu and P. Manneville, Phys. Rev. Fluids **4**, 113903 (2019).
- [20] F. Reetz, T. Kreilos, and T. M. Schneider, Nature communications **10**, 2277 (2019).
- [21] L. Klotz, G. Lemoult, K. Avila, and B. Hof, Phys. Rev. Lett. **128**, 014502 (2022).
- [22] P. V. Kashyap, Y. Duguet, and M. Chantry, Phys. Rev. Fluids **5**, 103902 (2020).
- [23] P. V. Kashyap, Y. Duguet, and O. Dauchot, Phys. Rev. Lett. **129**, 244501 (2022).

- [24] D. Coles and C. van Atta, AIAA Journal **4**, 1969 (1966).
- [25] G. Lemoult, L. Shi, K. Avila, S. V. Jalikop, M. Avila, and B. Hof, Nature Physics **12**, 254 (2016).
- [26] M. Chantry, L. S. Tuckerman, and D. Barkley, J. Fluid Mech. **824**, R1 (2017).
- [27] B. Hof, Nature Reviews Physics **5**, 62 (2023).
- [28] L. S. Tuckerman and D. Barkley, Phys. Fluids **23**, 041301 (2011).
- [29] P. Manneville, Europhysics Letters **98**, 64001 (2012).
- [30] S. Gomé, L. S. Tuckerman, and D. Barkley, J. Fluid Mech. **964**, A17 (2023).
- [31] M. Lagha and P. Manneville, Physics of Fluids **19**, 094105 (2007).
- [32] H.-Y. Shih, T.-L. Hsieh, and N. Goldenfeld, Nature Physics **12**, 245 (2016).
- [33] D. Barkley, Phys. Rev. E **84**, 016309 (2011).
- [34] D. Barkley, Journal of Physics: Conference Series **318**, 032001 (2011).
- [35] D. Barkley, J. Fluid Mech. **803**, P1 (2016).
- [36] G. Lemoult, K. Gumowski, J.-L. Aider, and J. E. Wesfreid, Eur. Phys. J. E **37**, 25 (2014).
- [37] X. Wang, H.-Y. Shih, and N. Goldenfeld, Phys. Rev. Lett. **129**, 034501 (2022).
- [38] K. Seshasayanan and P. Manneville, Fluid Dynamics Research **47**, 035512 (2015).
- [39] F. Waleffe, Phys. Fluids **9**, 883 (1997).
- [40] S. B. Pope, *Turbulent flows* (Cambridge university press, 2000).
- [41] B. Suri, J. Tithof, J. Mitchell, Radford, R. O. Grigoriev, and M. F. Schatz, Phys. Fluids **26**, 053601 (2014).
- [42] See Supplemental Material for a detailed description of the model derivation, linear stability analysis, and angle-selection calculations, and also movies showing (i) larger Reynolds numbers, (ii) larger domain sizes, and (iii) different aspect ratios.
- [43] K. J. Burns, G. M. Vasil, J. S. Oishi, D. Lecoanet, and B. P. Brown, Phys. Rev. Res. **2**, 023068 (2020).
- [44] S. J. Benavides, GitHub repository https://github.com/s-benavides/2D_MWF/, Commit: faabbd9ba8fadbe65b716667cab2bd7ba607b8e2 (2023).
- [45] A. Lundbladh and A. V. Johansson, J. Fluid Mech. **229**, 499 (1991).
- [46] J. Schumacher and B. Eckhardt, Phys. Rev. E **63**, 046307 (2001).
- [47] Z. Wang, C. Guet, R. Monchaux, Y. Duguet, and B. Eckhardt, J. Fluid Mech. **892**, A27 (2020).

- [48] M. Couliou and R. Monchaux, Phys. Rev. E **93**, 013108 (2016).
- [49] L. Klotz, A. Pavlenko, and J. Wesfreid, J. Fluid Mech. **912** (2021).
- [50] E. Marensi, G. Yalniz, and B. Hof, Dynamics and proliferation of turbulent stripes in channel and couette flow (2022), arXiv:2212.12406 [physics.flu-dyn].
- [51] P. Manneville, Fluid Dyn. Res. **44**, 031412 (2012).
- [52] J. Lu, J. Tao, and W. Zhou, Growth and decay of isolated turbulent band in plane-couette flow (2022), arXiv:2304.12409 [physics.flu-dyn].
- [53] P. V. Kashyap, Y. Duguet, and O. Dauchot, Entropy **22**, 1001 (2020).
- [54] A. Frishman and T. Grafke, Physical Review E **105**, 045108 (2022).
- [55] A. Frishman and T. Grafke, Proceedings of the Royal Society A **478**, 20220218 (2022).
- [56] J. Rolland, Phys. Rev. E **97**, 023109 (2018).
- [57] J. Rolland, J. Fluid Mech. **931**, A22 (2022).
- [58] S. Gomé, L. S. Tuckerman, and D. Barkley, Philosophical Transactions of the Royal Society A **380**, 20210036 (2022).

**Supplemental Material: Model for transitional turbulence in a
planar shear flow**

Santiago J. Benavides and Dwight Barkley

Mathematics Institute, University of Warwick,

Coventry CV4 7AL, United Kingdom

(Dated: September 4, 2023)

CONTENTS

I. Full Model Specification	3
II. Linear Stability Equations	4
III. Details of Model Derivation	5
A. Waleffe flow	5
B. Reynolds Average	6
C. Truncation of Vertical Modes	7
D. Turbulence Closures	9
1. Reynolds Stress	9
2. Production	10
3. Transport and Dissipation	10
4. q_1 and α	12
E. Parameter fits	13
IV. Details of Stability Analysis	14
A. Uniform steady states	14
B. Linearized equations	15
C. Normal-mode decomposition	16
D. Elimination of pressure and full eigenvalue problem	17
V. Angle Selection	18
A. Long-wavelength simplification	18
B. Critical angle at onset of instability	20
VI. Description of Supplemental Movies	23
References	24

I. FULL MODEL SPECIFICATION

The model is given by the following equations for the six fields $u_0, u_1, v_1, w_0, w_1, q_0$, each depending on streamwise coordinate x , spanwise coordinate z , and time t ,

$$\begin{aligned}
\frac{\partial u_0}{\partial t} + u_0 \partial_x u_0 + \frac{1}{2} u_1 \partial_x u_1 + \frac{1}{2} \beta v_1 u_1 + w_0 \partial_z u_0 + \frac{1}{2} w_1 \partial_z u_1 \\
= -\partial_x p_0 + \nabla_H^2 u_0 / Re - \alpha_0 u_0, \\
\frac{\partial u_1}{\partial t} + u_0 \partial_x u_1 + u_1 \partial_x u_0 + w_0 \partial_z u_1 + w_1 \partial_z u_0 \\
= -\partial_x p_1 + \nabla_H^2 u_1 / Re - (\alpha + \beta^2 / Re)(u_1 - 1) - \beta A(q_0), \\
\frac{\partial v_1}{\partial t} + u_0 \partial_x v_1 + w_0 \partial_z v_1 \\
= -\beta p_1 + \partial_x A(q_0) + \nabla_H^2 v_1 / Re - \beta^2 v_1 / Re, \\
\frac{\partial w_0}{\partial t} + u_0 \partial_x w_0 + \frac{1}{2} u_1 \partial_x w_1 + \frac{1}{2} \beta v_1 w_1 + w_0 \partial_z w_0 + \frac{1}{2} w_1 \partial_z w_1 \\
= -\partial_z p_0 + \nabla_H^2 w_0 / Re - \alpha_0 w_0, \\
\frac{\partial w_1}{\partial t} + u_0 \partial_x w_1 + u_1 \partial_x w_0 + w_0 \partial_z w_1 + w_1 \partial_z w_0 \\
= -\partial_z p_1 + \nabla_H^2 w_1 / Re - (\alpha + \beta^2 / Re)w_1, \\
\frac{\partial q_0}{\partial t} + u_0 \partial_x q_0 + \frac{1}{2} u_1 \partial_x q_1(u_1, w_1, q_0) + \frac{1}{2} \beta v_1 q_1(u_1, w_1, q_0) + w_0 \partial_z q_0 + \frac{1}{2} w_1 \partial_z q_1(u_1, w_1, q_0) \\
= \frac{1}{2} A(q_0)[\beta u_1 + \partial_x v_1] - 2\alpha q_0 - \varepsilon_0(q_0; Re) + \frac{1}{Re} \nabla_H^2 q_0 + \nabla_H \cdot (\nu_T(q_0; Re) \nabla_H q_0), \tag{1}
\end{aligned}$$

where $\beta = \pi/2$, and $\nabla_H = (\partial_x, \partial_z)$. The pressures p_0 and p_1 ensure incompressibility for each set of large-scale modes,

$$\partial_x u_0 + \partial_z w_0 = 0, \quad \partial_x u_1 - \beta v_1 + \partial_z w_1 = 0. \tag{2}$$

The equations are closed with the following,

$$\begin{aligned}
A(q_0) &= a((q_0^2 + \eta^2)^{1/2} - \eta), \quad \varepsilon_0(q_0; Re) = \frac{c}{Re} q_0, \\
q_1(u_1, w_1, q_0) &= -\frac{u_1 \partial_x q_0 + w_1 \partial_z q_0}{2\alpha + 2\kappa + \beta^2 / Re}, \quad \nu_T(q_0; Re) = d Re q_0. \tag{3}
\end{aligned}$$

Model parameters have the values

$$a = 0.3, c = 9.65, d = 0.05, \eta = 5 \times 10^{-3}, \alpha = 0.01, \alpha_0 = 0.03, \kappa = 0.045 \tag{4}$$

Since the model fields depend only on the horizontal spatial coordinates (x, z) , the notation ∇_H is redundant in stating the model. We use it to clearly distinguish ∇_H from the three-dimensional gradient $\nabla = (\partial_x, \partial_y, \partial_z)$ appearing in the derivation below.

II. LINEAR STABILITY EQUATIONS

The uniform turbulent state in the model is a steady state with no (x, z) dependence. These are of the form $(u_0, u_1, v_1, w_0, w_1, q_0) = (0, u_{ss}, 0, 0, 0, q_{ss})$, where u_{ss} and q_{ss} satisfy the u_1 and q_0 equations after dropping x, z , and t derivatives:

$$0 = (\alpha + \beta^2/Re)(1 - u_{ss}) - \beta A(q_{ss}), \quad (5a)$$

$$0 = \frac{1}{2}A(q_{ss})\beta u_{ss} - 2\alpha q_{ss} - \varepsilon_0(q_{ss}; Re). \quad (5b)$$

We denote uniform steady states by (u_{ss}, q_{ss}) .

Straightforward linearization about the uniform turbulent state gives the following eigenvalue problem for the temporal growth rate σ of a linear mode $\hat{u}_0 \exp(ik_x x + ik_z z)$, and similarly for $\hat{u}_1, \hat{v}_1, \hat{w}_0, \hat{w}_1, \hat{q}_0$.

$$\sigma \hat{u}_0 + \frac{1}{2}ik_x u_{ss} \hat{u}_1 + \frac{1}{2}\beta u_{ss} \hat{v}_1 = \frac{k_x^2 \beta u_{ss}}{k^2} \hat{v}_1 + \left(\hat{D}_2 - \alpha_0 \right) \hat{u}_0 \quad (6a)$$

$$\sigma \hat{u}_1 + ik_x u_{ss} \hat{u}_0 = -\frac{ik_x \alpha \beta}{k^2 + \beta^2} \hat{v}_1 + \left(\hat{D}_3 - \alpha \right) \hat{u}_1 + \left(\frac{2k_x^2}{k^2 + \beta^2} - 1 \right) \beta \delta A_{ss} \hat{q}_0 \quad (6b)$$

$$\sigma \hat{v}_1 = \left(\hat{D}_3 - \frac{\alpha \beta^2}{k^2 + \beta^2} \right) \hat{v}_1 + \left(1 - \frac{2\beta^2}{k^2 + \beta^2} \right) ik_x \delta A_{ss} \hat{q}_0 \quad (6c)$$

$$\sigma \hat{w}_0 + \frac{1}{2}ik_x u_{ss} \hat{w}_1 = \frac{k_x k_z \beta u_{ss}}{k^2} \hat{v}_1 + \left(\hat{D}_2 - \alpha_0 \right) \hat{w}_0 \quad (6d)$$

$$\sigma \hat{w}_1 + u_{ss} ik_x \hat{w}_0 = -\frac{ik_z \alpha \beta}{k^2 + \beta^2} \hat{v}_1 + \left(\hat{D}_3 - \alpha \right) \hat{w}_1 + \frac{2k_x k_z \beta \delta A_{ss}}{k^2 + \beta^2} \hat{q}_0 \quad (6e)$$

$$\sigma \hat{q}_0 = \frac{1}{2}A_{ss} (\beta \hat{u}_1 + ik_x \hat{v}_1) + \hat{L} \hat{q}_0 \quad (6f)$$

where

$$k^2 = k_x^2 + k_z^2, \quad \hat{D}_2 = -\frac{k^2}{Re}, \quad \hat{D}_3 = -\frac{k^2 + \beta^2}{Re}, \quad (7)$$

$$A_{ss} \equiv A(u_{ss}, q_{ss}), \quad \delta A_{ss} \equiv \frac{\partial A}{\partial q_0}(q_{ss}), \quad \delta \varepsilon_{ss} = \frac{d\varepsilon_0}{dq_0}(q_{ss}, Re), \quad (8)$$

$$\hat{L} = \frac{1}{2}\beta u_{ss} \delta A_{ss} - 2\alpha - \delta \varepsilon_{ss} - \frac{k^2}{Re} - \nu_T(q_{ss}; Re)k^2 - \frac{u_{ss}^2 k_x^2}{2(2\alpha + 2\kappa + \beta^2/Re)}. \quad (9)$$

See Sec. IV for further details.

For numerical computation of the growth rate σ in the main paper, all terms except those involving σ are put onto the right-hand side. The eigenvalue problem becomes $\sigma\mathbf{x} = \mathbf{M}\mathbf{x}$, where $\mathbf{x} = (\hat{u}_0, \hat{u}_1, \hat{v}_1, \hat{w}_0, \hat{w}_1, \hat{q}_0)^T$ and \mathbf{M} is a 6×6 matrix. Given parameters Re , k_x , and k_z , and (u_{ss}, q_{ss}) from a numerical solution of (5), the elements of \mathbf{M} are obtained. The eigenvalues of \mathbf{M} are found from a standard eigenvalue solver. The leading eigenvalue, corresponding to maximum growth rate, is always found to be real.

III. DETAILS OF MODEL DERIVATION

In this section, we will walk through the model derivation. The general approach for the model creation will be the following: first we will present the Reynolds-Averaged Navier Stokes (RANS) equations, along with the equation for the Turbulent Kinetic Energy (TKE). These will constitute our main dynamical variables. We will then introduce our simplification assumptions and turbulence closures, all of which were motivated (and validated) by observations from direct numerical simulations.

A. Waleffe flow

We start from a planar flow confined between stress-free boundaries and driven by a sinusoidal body force. In the wall-bounded literature this system is called Waleffe flow (Wf), after Waleffe who used it in his work on the self-sustaining process [1]. The flow reproduces the same transitional phenomena as plane Couette flow (pCf) [2, 3], while the stress-free boundary conditions significantly simplifying analytical and computational treatment.

We use coordinates (x, y, z) aligned with the streamwise, wall-normal, and spanwise directions, respectively. The components of the velocity $\tilde{\mathbf{u}}$ are denoted by $(\tilde{u}, \tilde{v}, \tilde{w})$. We non-dimensionalize using a length scale h equal to the half gap between the stress-free walls, and a velocity scale U , equal to the maximum laminar velocity. In non-dimensional coordinates, the walls are at $y = \pm 1$. We use $\beta \equiv \pi/2$ as a shorthand for the first wall-normal (vertical) wavenumber. The momentum equation for Wf is,

$$\frac{\partial \tilde{\mathbf{u}}}{\partial t} + \tilde{\mathbf{u}} \cdot \nabla \tilde{\mathbf{u}} = -\nabla \tilde{p} + \frac{1}{Re} \nabla^2 \tilde{\mathbf{u}} - \alpha \tilde{\mathbf{u}}_H + \mathbf{F}, \quad (10)$$

where \tilde{p} is the pressure, $Re \equiv Uh/\nu$ is the Reynolds number, ν is the kinematic viscosity, \mathbf{F} is the body force, and α is the drag coefficient. The drag term only acts on the horizontal velocity components $\tilde{\mathbf{u}}_H \equiv \tilde{u}\mathbf{e}_x + \tilde{w}\mathbf{e}_z$ and is only a significant source of dissipation for y -independent modes and large horizontal scales. It represents the effect of the no-slip boundary conditions in pCf, which acts as an effective drag on the y -averaged horizontal velocities [3, 4]. The body force is defined to be,

$$\mathbf{F} \equiv \left(\alpha + \frac{\beta^2}{Re} \right) \sin(\beta y) \mathbf{e}_x. \quad (11)$$

This body force results in a (linearly stable) laminar solution of the form $\tilde{\mathbf{u}}_{lam} = \sin(\beta y)\mathbf{e}_x$. The momentum equation is accompanied by an incompressibility condition

$$\nabla \cdot \tilde{\mathbf{u}} = 0, \quad (12)$$

periodic boundary conditions in the horizontal (x, z) directions, and stress-free boundary conditions in the vertical direction

$$\partial_y \tilde{u}(x, \pm 1, z) = \tilde{v}(x, \pm 1, z) = \partial_y \tilde{w}(x, \pm 1, z) = 0, \quad (13)$$

which includes a no-penetration condition on the wall-normal velocity.

Throughout this work, we will use direct numerical simulations (DNS) of Wf as a way to motivate model choices and calibrate parameter values in our model. We simulated the Wf equations (with periodic boundary conditions in the horizontal) using the open source pseudo-spectral code Dedalus [5]. A first-order Crank-Nicolson Adams-Basforth time stepping scheme was used with a time step $\Delta t = 0.003$ advective time units. A Fourier-spectral method with 3/2 dealiasing is used for the horizontal directions, with a resolution of eight grid points per space unit. A SinCos basis was used in the vertical direction with the same spatial resolution. Random initial conditions were used at higher Re and the banded solution was found by incrementally decreasing Re from the resulting uniform state.

B. Reynolds Average

We apply a Reynolds average to the momentum equation by letting $\tilde{\mathbf{u}} = \mathbf{u} + \mathbf{u}'$, where $\mathbf{u} \equiv \langle \tilde{\mathbf{u}} \rangle$ is the average of the velocity field and $\langle \mathbf{u}' \rangle = 0$. We do not specify the averaging operation, although presumably it is either a temporal average or spatial coarse graining

such that scales smaller than h , as well as the turbulent space and time scales, are averaged over, leading to slowly evolving, non-fluctuating large scale quantities. For this reason, we will refer to \mathbf{u} as the ‘large-scale flow’. We also define the Turbulent Kinetic Energy (TKE) $q \equiv \langle \mathbf{u}' \cdot \mathbf{u}' \rangle / 2$. Following standard procedures [6], we arrive at the equations of motion for the large-scale flow,

$$\frac{\partial \mathbf{u}}{\partial t} + \mathbf{u} \cdot \nabla \mathbf{u} = -\nabla p + \frac{1}{Re} \nabla^2 \mathbf{u} - \alpha \mathbf{u}_H + \mathbf{F} + \nabla \cdot \mathcal{R}, \quad (14a)$$

and TKE,

$$\frac{\partial q}{\partial t} + \mathbf{u} \cdot \nabla q + \nabla \cdot \mathbf{T} = \mathcal{P} - \varepsilon + \frac{1}{Re} \nabla^2 q - 2\alpha q, \quad (14b)$$

where \mathbf{u} satisfies the same incompressibility constraint and boundary conditions as $\tilde{\mathbf{u}}$, equations (12) and (13). The TKE also has vanishing gradients at the two walls.

A small approximation is already made in equation (14b). The exact drag term from averaging is $\alpha \langle (u')^2 + (w')^2 \rangle$, and we have approximated it as $2\alpha q = \alpha \langle (u')^2 + (v')^2 + (w')^2 \rangle$. Since $\langle (v')^2 \rangle \ll \langle (u')^2 + (w')^2 \rangle$, this approximation has negligible effect.

The averaging has introduced four new fluctuation correlation terms that will eventually require closure choices. These are the Reynolds stress,

$$\mathcal{R}_{ij} = -\langle u'_i u'_j \rangle, \quad (15)$$

the production term,

$$\mathcal{P} = -\langle u'_i u'_j \rangle \partial_j u_i, \quad (16)$$

the pseudo-dissipation rate,

$$\varepsilon = \frac{1}{Re} |\nabla \mathbf{u}'|^2, \quad (17)$$

and the transport term,

$$T_i = \frac{1}{2} \langle u'_i u'_j u'_j \rangle + \frac{1}{2} \langle u'_i p' \rangle. \quad (18)$$

We use the Einstein summation convention, with u_i representing an indexing of u, v, w and similarly for u'_i . Note that closing the Reynolds stress term also closes the production term.

C. Truncation of Vertical Modes

We turn to modeling and continue to use variables \mathbf{u} and q , rather than introducing separate notation for the model. Our first step is to introduce a Galerkin truncation in the

vertical direction. Given the sinusoidal body force \mathbf{F} , corresponding sinusoidal laminar flow, and the stress-free boundary conditions, we use a Fourier basis and project onto the first two vertical modes (that is, the y -independent and $\sin(\beta y)$ or $\cos(\beta y)$ modes). The model large-scale flow and TKE are represented by

$$u(x, y, z, t) = u_0(x, z, t) + u_1(x, z, t) \sin(\beta y), \quad (19a)$$

$$v(x, y, z, t) = v_1(x, z, t) \cos(\beta y), \quad (19b)$$

$$w(x, y, z, t) = w_0(x, z, t) + w_1(x, z, t) \sin(\beta y), \quad (19c)$$

$$q(x, y, z, t) = q_0(x, z, t) + q_1(x, z, t) \sin(\beta y), \quad (19d)$$

The no-penetration condition $v(x, \pm 1, z) = 0$ implies $v_0 = 0$ and that the lowest v -mode goes as cosine. Incompressibility of the large-scale flow, $\nabla \cdot \mathbf{u} = 0$, becomes two statements

$$\partial_x u_0 + \partial_z w_0 = 0, \quad \partial_x u_1 - \beta v_1 + \partial_z w_1 = 0.$$

The pressure field p in (14a) that enforces incompressibility is represented in the form $p(x, y, z, t) = p_0(x, z, t) + p_1(x, z, t) \sin(\beta y)$. The fields p_0 and p_1 separately ensure incompressibility for each set of large-scale modes. Although every fluctuation correlation term has an equivalent decomposition in vertical modes, ε is the only one that will require the consideration of both vertical modes (see the next section below). Because of this we explicitly define $\varepsilon = \varepsilon_0(x, z, t) + \varepsilon_1(x, z, t) \sin(\beta y)$, but will not expand the remaining fluctuation correlation terms in terms of vertical modes. Instead, we will write their y -dependence directly.

While v_1 is small, it is essential for the flow dynamics and the retained modes are the minimal set describing a three-dimensional vector field. For the TKE field, q_0 represents the y -averaged turbulence and q_1 allows for different levels of turbulence in the upper and lower halves of the geometry. This is important in capturing the so-called ‘overhangs’ at the edges of turbulent bands where turbulence is not vertically uniform due to the mean shear. Finally, DNS of Wf confirms that the modes in (14) are the most energetic modes present in turbulent bands. It is therefore reasonable to base our model on this minimal set of modes. Substitution of (19) into (14), followed by a Galerkin projection, will give evolution equations for the fields, but first we need to consider the turbulence closures.

D. Turbulence Closures

We will now present the closures. These will be based on fully-resolved simulations and four-mode simulations of Wf from previous work [2], as well as simulations performed by the authors for the current study.

1. Reynolds Stress

We start with the Reynolds stress tensor. Only two terms play a significant role in the dynamics, namely $-\langle u'u' \rangle$ and $-\langle u'v' \rangle$. Fully-resolved simulations reveal only one dominant vertical mode in each of these Reynolds stress tensor components – the zeroth vertical mode (invariant in y) for $-\langle u'u' \rangle$ and the first vertical mode for $-\langle u'v' \rangle$. The latter fact can be seen clearly in Figure 4 of Chantry *et al.* (2016) [2]. It is assumed that the amplitudes of these terms depend only on the TKE and have the form:

$$\mathcal{R}_{12} = \mathcal{R}_{21} = -\langle u'v' \rangle = A(q) \cos(\beta y), \quad (20)$$

$$\mathcal{R}_{11} = -\langle u'u' \rangle = -B(q). \quad (21)$$

This results in two Reynolds-stress body forces – one in the streamwise direction x , and one in the wall-normal direction y :

$$\nabla \cdot \mathcal{R} = (-\partial_x B(q) - A(q)\beta \sin(\beta y)) \mathbf{e}_x + (\cos(\beta y) \partial_x A(q)) \mathbf{e}_y. \quad (22)$$

We have chosen the signs so that $A(q), B(q) > 0$.

We now neglect the $-\langle u'u' \rangle$ stress, and take $B(q) = 0$ for the remainder. The reason we have included it in the discussion to this point is because this stress accounts for the largest effect that we have measured in DNS that we do not include in the present model. This stress couples the u_0 field to q_0 and q_1 . Its associated Reynolds stress force acts to reduce the amplitude of u_0 , while its associated production term increase q_0 (its effect is small compared to other production terms). We have briefly investigated the role of this stress in the model and have found that including it does not alter the model dynamics in a significant way. Therefore, for simplicity we neglect it in the present model. However, since it is not a negligible term in the u_0 equation, this has contributed to the need for an increased drag coefficient α_0 (see III D 4). Future studies may wish to include it. (We find that taking $B(q)$ linear in q is a reasonable approximation.)

Since $A(q)$ is the amplitude of an even mode in y , it can only depend on the even part of the TKE field, that is q_0 in our model expansion. The Reynolds-stress closure is specified by a function $A(q_0)$. We use the following,

$$A(q_0) = a((q_0^2 + \eta^2)^{1/2} - \eta), \quad (23)$$

where a and η are parameters with η small. For $q_0 \gg \eta$, $A(q_0) \approx aq_0$, meaning that \mathcal{R}_{01} is simply proportional to the TKE. From DNS, we find that $A(q_0)$ scales with a slightly larger exponent, (approximately $q_0^{1.2}$) and does depend somewhat on Re , but for simplicity we choose not to take these factors into account in the simple model. For small q_0 , we have $A(q_0) \approx aq_0^2/(2\eta)$, and $A(q_0)$ goes to zero quadratically in q_0 . This serves to cut off turbulent production at small q_0 (see section III D 3). Supplemental Fig. 1(c) compares DNS-measured values of the Reynolds stress force across a band with our closure, as well as with the resulting force across the band from model simulations (Fig. 2 (a) $t = 25350$ in the main text).

2. Production

The production \mathcal{P} is just the contraction of the Reynolds stress tensor \mathcal{R} and large-scale velocity gradient tensor $\nabla \mathbf{u}$, followed by projection back to the q equation. Given our simplification of \mathcal{R} , the only terms are $\mathcal{R}_{12}\partial_y u + \mathcal{R}_{21}\partial_x v$. Using our expansions and projecting back to the retained modes gives

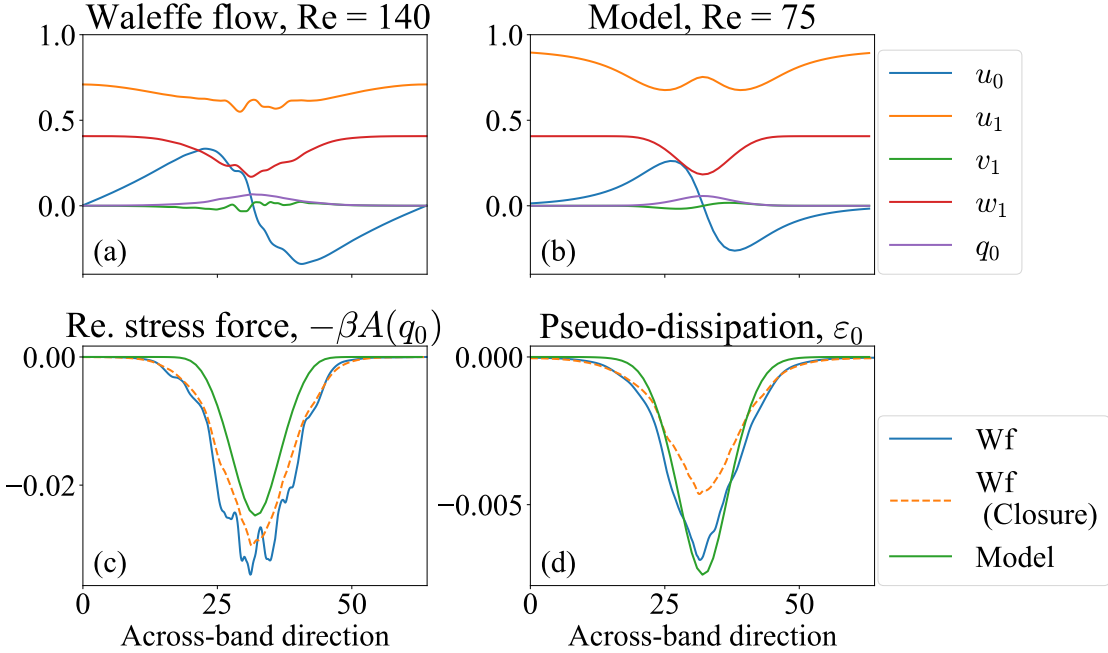
$$\mathcal{P} = \frac{1}{2}A(q_0)[\beta u_1 + \partial_x v_1].$$

It is constant in y and only couples to q_0 .

3. Transport and Dissipation

There are two closures left in the TKE equation, the turbulent pseudo-dissipation rate and the turbulent transport term. We first focus on the pseudo-dissipation, where we look at both vertical modes separately, and end with the turbulent transport term.

As with A , the pseudo-dissipation rate ε_0 must only depend on q_0 , and we further assume that is linear in q_0 . DNS and model tests confirm that this approximation is adequate



Supplemental Fig. 1. Comparison of turbulent band profiles and closures between a DNS of Wf at $Re = 140$ (averaged for 500 time units) and our model at $Re = 75$ (steady state). Across-band profiles of vertical mode amplitudes for the DNS, (a), and for the model (b). Panel (c) shows the Reynold stress force for the u_1 mode equation, measured directly from the DNS at $Re = 140$ (blue), its closure (dashed, orange), and the corresponding Reynolds stress force for the model (green) at $Re = 75$. Panel (d) shows a similar plot but for the pseudo-dissipation rate.

(Supplemental Fig. 1 (d)), and they also inform us on the Reynolds number dependence of the coefficient (found by matching (u_{ss}, q_{ss}) with DNS as best as possible for multiple values of Re). Our closure for ε_0 is,

$$\varepsilon_0(q_0; Re) = \frac{c}{Re} q_0, \quad (24)$$

where c is a parameter. Note that in the main paper, we lighten notation by dropping the 0 subscript from ε_0 , and write simply $\varepsilon(q_0; Re) = cq_0/Re$.

Having specified the dissipation, we can comment on the functional form of $A(q_0)$. The dependence of $A(q_0)$ on q_0 gives a quadratic cutoff in production as $q_0 \rightarrow 0$. Since ε_0 is linear in q_0 , production will necessarily fall below dissipation at small q_0 . This ensures stability of laminar flow to small perturbations in q_0 . Physically this rules out “infinitesimal turbulence”, accounting for the fact that very small fluctuations (deviations from laminar flow), are not turbulent but rather are small laminar disturbances that we know do not

sustain nonlinearly.

A similarly simple closure exists for $\varepsilon_1(q)$, that is $\varepsilon_1(q_1) = 2\kappa q_1$, where κ does not depend on Re . Although we have measured κ from the pseudo-dissipation rate of a DNS, and not a transport term, this closure can be seen intuitively as the vertical (turbulent) diffusion of turbulence, modeled as a ‘drag’ term with drag coefficient κ in a two-layer simplification of our system, such that $\varepsilon_{top} = -\kappa(q_{top} - q_{bottom})$ and $\varepsilon_{bottom} = -\kappa(q_{bottom} - q_{top})$ [7].

Moving on to the transport term, DNS results and model tests suggest that only the zeroth vertical mode of the transport term plays a significant role in the turbulence budget. Apart from this simplification in vertical mode number, we invoke the gradient-diffusion hypothesis [6, Section 10.3] which states that,

$$\mathbf{T}(q_0; Re) = -\nu_T(q_0; Re)\nabla_H q_0. \quad (25)$$

We have again used the fact that, since \mathbf{T} does not depend on y , it must only be a function of q_0 . The turbulent diffusivity is defined in a standard way, following Pope [6, Section 10.3], as $\nu_T \propto q_0^2/\varepsilon_0$. Since we’ve already assumed that $\varepsilon_0 = cq_0/Re$, we can then substitute this into the turbulent diffusivity arriving at,

$$\nu_T(q_0; Re) = d Re q_0. \quad (26)$$

4. q_1 and α

We make two final model approximations. The first concerns q_1 . Projecting the TKE dynamics (14b) into the $\sin(\beta y)$ mode gives the evolution equation for q_1 . Ignoring streamwise and spanwise derivatives of q_1 (which we have verified with DNS), the q_1 equation simplifies to,

$$\frac{\partial q_1}{\partial t} + u_1 \partial_x q_0 + w_1 \partial_z q_0 = -(2\alpha + \beta^2/Re)q_1 - 2\kappa q_1. \quad (27)$$

In an effort to achieve the simplest possible model, we assume that the timescales of q_1 are short, resulting in an adiabatic condition for q_1 . Setting $\partial_t q_1 = 0$, we can express q_1 as a function of \mathbf{u}_H and q_0 ,

$$q_1(u_1, w_1, q_0) = -\frac{u_1 \partial_x q_0 + w_1 \partial_z q_0}{2\alpha + 2\kappa + \beta^2/Re}. \quad (28)$$

Thus, q_1 is not treated as a dynamical field in our model.

The last model approximation we make is to use a larger value of α in the u_0, w_0 equations. In the process of neglecting $\langle u'u' \rangle$, which plays a significant role in the budget of u_0 , we found it necessary to increase the drag for the zero modes of the large-scale flow. Furthermore, we found that, without this increase, the large-scale flow has a larger tendency to become unstable and chaotic, making the banded state unattainable. We therefore introduce a final model parameter α_0 to use in the u_0, w_0 equations.

E. Parameter fits

The numerical value of the parameters were first calibrated using measurements of the Reynolds stresses, turbulent dissipation, and transport term in a time and along-band average of a single turbulent band found in a Wf simulation run at $Re = 140$ (Supplemental Fig. 1(a)). Due to the severe nature of our simplifications and assumptions in our closure choices, we had to further refine these parameter values in order to ensure simulation results which better matched those of the DNS (Supplemental Fig. 1(b)).

The first step in choosing parameter values was measuring the Reynolds stress amplitudes, turbulent dissipation, and turbulent diffusion in a DNS, giving us a first estimate for what the coefficients in our closures should be. From there, we tweaked a and c so that the uniform turbulent fixed point in the homogeneous dynamics (subsection IV A) would appear at $Re = 72$, a value which we found results in turbulent bands at about $Re = 68$. Despite being able to arbitrarily choose the Reynolds number corresponding to the appearance of bands in our model, the one we have settled on is about half of that for Wf ($Re \approx 130$). Our attempts at having realistic Wf Reynolds numbers resulted in the formation of sharp gradients in the large-scale flow which caused numerical instability, as well as the nonlinear evolution being more prone to instability and chaos, resulting in a lack of banded states. Although our DNS budgets don't suggest that a turbulent viscosity plays a significant role, the lower Re values chosen could be interpreted in such a way.

After calibrating a and c , we performed a series of simulations of the model in a simplified geometry, following that of the ‘tilted’ domain simulations from Barkley & Tuckerman [8], except restricted to a one-dimensional domain. That is, a domain tilted at a fixed angle (24 degrees in our case) to the streamwise direction, extended in the across-band direction but assumed to be invariant in the along-band direction, making it a one-dimensional calculation.

We performed a series of simulations in this setup to observe the formation of bands, measure the large scale flow and TKE amplitudes, as well as the width of the bands. From these 1D runs, we modified the rest of the parameters, in particular the turbulent diffusivity coefficient d , so as to best match the band width found in the DNS.

The final check on the parameter choices was to run a 2D simulation of the full equations (1) and observe the behavior. Throughout our experimentation with parameter values, we found that the presence of a linear instability of the spatially uniform steady state, the formation and stability of bands in the 1D model, and the angle of the initial bands in the 2D model all to be extremely robust. However, the two-dimensional dynamics of the full model proved to be more sensitive to parameter values. In particular, we found various instabilities of the turbulent bands in the along-band direction, as well as instances when the large scale flow's amplitude was too large, resulting in chaotic motion. This restricted our parameter values, ultimately resulting in our introduction of α_0 as well as a forced mismatch between observed Reynolds number transitions in the DNS and in our model.

IV. DETAILS OF STABILITY ANALYSIS

In this section we analyze the stability of the the uniform turbulent state in the model system. The content is standard, straightforward linear stability analysis, but since there are many steps in the calculations, for completeness we present a summary of key steps.

A. Uniform steady states

The uniform turbulent state in the model is a steady state, or fixed point, of the equations with no (x, z) dependence. Dropping all horizontal derivatives from the model equations, it is immediately evident that any uniform steady state must have $u_0 = w_0 = v_1 = w_1 = 0$, and hence uniform steady states can have at most u_1 and q_0 different from zero. We denote uniform steady states by (u_{ss}, q_{ss}) , where u_{ss} and q_{ss} satisfy the u_1 and q_0 equations after dropping x, z , and t derivatives:

$$0 = (\alpha + \beta^2/Re)(1 - u_{ss}) - \beta A(q_{ss}), \quad (29a)$$

$$0 = \frac{1}{2}A(q_{ss})\beta u_{ss} - 2\alpha q_{ss} - \varepsilon_0(q_{ss}; Re). \quad (29b)$$

One sees that laminar flow, $(u_{ss}, q_{ss}) = (1, 0)$, is a solution to these equations for any positive Re . We are primarily concerned with the non-trivial steady states with $(u_{ss}, q_{ss}) \neq (1, 0)$ corresponding to uniform turbulence. For $Re > 72.4$, a pair of non-trivial steady states exist, with $u_{ss} < 1$ and $q_{ss} > 0$, corresponding to uniform turbulence. One of these states (the ‘upper state’) is stable to spatially uniform perturbations.

B. Linearized equations

Linear stability of (u_{ss}, q_{ss}) is determined by first linearizing the model equations about this state. Using primes to denote perturbation fields, we let

$$u_0 = u'_0, w_0 = w'_0, \quad (30)$$

$$u_1 = u_{ss} + u'_1, v_1 = v'_1, w_1 = w'_1 \quad (31)$$

$$q_0 = q_{ss} + q'_0, \quad (32)$$

and substitute these into the model equations and then drop terms quadratic in the prime variables. Initially, it will be convenient to consider the linearized equation in three groups: the vertical mode-0 large-scale-flow fields, the vertical mode-1 large-scale-flow fields, and the turbulent field. We define two operators corresponding to the viscous diffusion terms

$$D_2 \equiv \frac{1}{Re} \nabla_H^2 \quad (33)$$

$$D_3 \equiv \frac{1}{Re} (\nabla_H^2 - \beta^2) \quad (34)$$

The vertical mode-0 linear equations are

$$\frac{\partial u'_0}{\partial t} + \frac{1}{2} u_{ss} \frac{\partial u'_1}{\partial x} + \frac{1}{2} \beta u_{ss} v'_1 = - \frac{\partial p'_0}{\partial x} + D_2 u'_0 - \alpha_0 u'_0 \quad (35)$$

$$\frac{\partial w'_0}{\partial t} + \frac{1}{2} u_{ss} \frac{\partial w'_1}{\partial x} = - \frac{\partial p'_0}{\partial z} + D_2 w'_0 - \alpha_0 w'_0 \quad (36)$$

$$\frac{\partial u'_0}{\partial x} + \frac{\partial w'_0}{\partial z} = 0 \quad (37)$$

where p'_0 is the perturbation pressure needed to maintain incompressibility in the perturbation fields.

The vertical mode-1 linear equations are

$$\frac{\partial u'_1}{\partial t} + u_{ss} \frac{\partial u'_0}{\partial x} = - \frac{\partial p'_1}{\partial x} + D_3 u'_1 - \alpha u'_1 - \beta \delta A_{ss} q'_0 \quad (38)$$

$$\frac{\partial v'_1}{\partial t} = - \beta p'_1 + D_3 v'_1 + \delta A_{ss} \frac{\partial q'_0}{\partial x} \quad (39)$$

$$\frac{\partial w'_1}{\partial t} + u_{ss} \frac{\partial w'_0}{\partial x} = - \frac{\partial p'_1}{\partial z} + D_3 w'_1 - \alpha w'_1 \quad (40)$$

$$\frac{\partial u'_1}{\partial x} - \beta v'_1 + \frac{\partial w'_1}{\partial z} = 0 \quad (41)$$

where p'_1 is the perturbation pressure needed to maintain incompressibility and

$$\delta A_{ss} \equiv \frac{\partial A}{\partial q_0}(q_{ss}) \quad (42)$$

The linearized turbulent field equation is

$$\frac{\partial q'_0}{\partial t} = \frac{1}{2} A_{ss} \left(\beta u'_1 + \frac{\partial v'_1}{\partial x} \right) + L q'_0 \quad (43)$$

where

$$A_{ss} \equiv A(u_{ss}, q_{ss}) \quad (44)$$

and L is the operator

$$\begin{aligned} L \equiv & \frac{1}{2} \beta u_{ss} \delta A_{ss} - 2\alpha - \delta \varepsilon_{ss} \\ & + \frac{1}{Re} \nabla_H^2 + \nu_T(q_{ss}; Re) \nabla_H^2 + \frac{u_{ss}^2}{2(2\alpha + 2\kappa + \beta^2/Re)} \frac{\partial^2}{\partial x^2} \end{aligned} \quad (45)$$

with

$$\delta \varepsilon_{ss} = \frac{d\varepsilon_0}{dq_0}(q_{ss}, Re).$$

We will discuss the important operator L below.

C. Normal-mode decomposition

We next employ a spectral normal-mode decomposition to transform the differential operators into algebraic form. Let

$$u'_0 = \hat{u}_0 e^{i(k_x x + k_z z)} e^{\sigma t} \quad (46)$$

and similarly for the other fields, where k_x and k_z are the wavenumbers of the normal modes and σ is a temporal eigenvalue to be determined. In principle σ may be complex. Upon substitution we obtain the following.

The vertical mode-0 linear equations become

$$\sigma\hat{u}_0 + \frac{1}{2}u_{ss}ik_x\hat{u}_1 + \frac{1}{2}\beta u_{ss}\hat{v}_1 = -ik_x\hat{p}_0 + \hat{D}_2\hat{u}_0 - \alpha_0\hat{u}_0 \quad (47)$$

$$\sigma\hat{w}_0 + \frac{1}{2}u_{ss}ik_x\hat{w}_1 = -ik_z\hat{p}_0 + \hat{D}_2\hat{w}_0 - \alpha_0\hat{w}_0 \quad (48)$$

$$ik_x\hat{u}_0 + ik_z\hat{w}_0 = 0 \quad (49)$$

where

$$\hat{D}_2 = -\frac{k_x^2 + k_z^2}{Re} = -\frac{k^2}{Re} \quad (50)$$

The vertical mode-1 linear equations become

$$\sigma\hat{u}_1 + u_{ss}ik_x\hat{u}_0 = -ik_x\hat{p}_1 + \hat{D}_3\hat{u}_1 - \alpha\hat{u}_1 - \beta\delta A_{ss}\hat{q}_0 \quad (51)$$

$$\sigma\hat{v}_1 = -\beta\hat{p}_1 + \hat{D}_3\hat{v}_1 + \delta A_{ss}ik_x\hat{q}_0 \quad (52)$$

$$\sigma\hat{w}_1 + u_{ss}ik_x\hat{w}_0 = -ik_z\hat{p}_1 + \hat{D}_3\hat{w}_1 - \alpha\hat{w}_1 \quad (53)$$

$$ik_x\hat{u}_1 - \beta\hat{v}_1 + ik_z\hat{w}_1 = 0 \quad (54)$$

where

$$\hat{D}_3 = -\frac{k_x^2 + k_z^2 + \beta^2}{Re} = -\frac{k^2 + \beta^2}{Re} \quad (55)$$

The turbulent-field equation becomes

$$\sigma\hat{q}_0 = \frac{1}{2}A_{ss}(\beta\hat{u}_1 + ik_x\hat{v}_1) + \hat{L}\hat{q}_0 \quad (56)$$

where \hat{L} is obtained from (45) by replacing $(\partial_x, \partial_z) \rightarrow (ik_x, ik_z)$.

D. Elimination of pressure and full eigenvalue problem

We use incompressibility to obtain expressions for the pressure fields \hat{p}_0 and \hat{p}_1 . Multiplying (47) by ik_x and (48) by ik_z , adding these, and using the incompressibility constraints (49) and (54), one obtains the following expression for \hat{p}_0

$$\hat{p}_0 = \frac{ik_x\beta u_{ss}}{k^2} \hat{v}_1 \quad (57)$$

Similarly, multiplying (51), (52), and (53), by ik_x , $-\beta$, and ik_z , respectively and using incompressibility, one obtains

$$\hat{p}_1 = \frac{2ik_x\beta\delta A_{ss}}{k^2 + \beta^2} \hat{q}_0 + \frac{\alpha\beta}{k^2 + \beta^2} \hat{v}_1 \quad (58)$$

Substituting these expressions for pressure, we obtain the following full eigenvalue problem for the temporal growth rate σ

$$\sigma \hat{u}_0 + \frac{1}{2} ik_x u_{ss} \hat{u}_1 + \frac{1}{2} \beta u_{ss} \hat{v}_1 = \frac{k_x^2 \beta u_{ss}}{k^2} \hat{v}_1 + (\hat{D}_2 - \alpha_0) \hat{u}_0 \quad (59a)$$

$$\sigma \hat{u}_1 + ik_x u_{ss} \hat{u}_0 = -\frac{ik_x \alpha \beta}{k^2 + \beta^2} \hat{v}_1 + (\hat{D}_3 - \alpha) \hat{u}_1 + \left(\frac{2k_x^2}{k^2 + \beta^2} - 1 \right) \beta \delta A_{ss} \hat{q}_0 \quad (59b)$$

$$\sigma \hat{v}_1 = \left(\hat{D}_3 - \frac{\alpha \beta^2}{k^2 + \beta^2} \right) \hat{v}_1 + \left(1 - \frac{2\beta^2}{k^2 + \beta^2} \right) ik_x \delta A_{ss} \hat{q}_0 \quad (59c)$$

$$\sigma \hat{w}_0 + \frac{1}{2} ik_x u_{ss} \hat{w}_1 = \frac{k_x k_z \beta u_{ss}}{k^2} \hat{v}_1 + (\hat{D}_2 - \alpha_0) \hat{w}_0 \quad (59d)$$

$$\sigma \hat{w}_1 + u_{ss} ik_x \hat{w}_0 = -\frac{ik_z \alpha \beta}{k^2 + \beta^2} \hat{v}_1 + (\hat{D}_3 - \alpha) \hat{w}_1 + \frac{2k_x k_z \beta \delta A_{ss}}{k^2 + \beta^2} \hat{q}_0 \quad (59e)$$

$$\sigma \hat{q}_0 = \frac{1}{2} A_{ss} (\beta \hat{u}_1 + ik_x \hat{v}_1) + \hat{L} \hat{q}_0 \quad (59f)$$

We have written these equations such as to indicate the origins of terms. Those on the left are associated with advection, while those on the right are associated with pressure gradients, dissipative effects and turbulent production. The five terms shown in red can be neglected for long-wavelength (small- k) modes as discussed below.

V. ANGLE SELECTION

In this section we consider the selected angle of turbulent bands at onset of instability of uniform turbulence as Re is decreased. We first consider a simplification of the linear stability equations for modes with long-wavelengths relative to the wall spacing. We then show explicitly that in this long-wavelength case that the selected angle of turbulent bands at onset, the critical angle, is necessarily less than 45° .

A. Long-wavelength simplification

Turbulent bands have long wavelengths relative to the wall spacing, which by choice of length scales is $2h = 2$. Considering long-wavelength modes allows us to simplify the linear stability equations. Letting the wavenumber be $k = \epsilon \ll 1$, we will drop terms in the eigenvalue problem (59) that are $O(\epsilon^2)$.

While α is a small parameter, we assume that α is no smaller than ϵ . Thus, we make the approximations

$$k^2 + \beta^2 \rightarrow \beta^2, \quad (60)$$

$$\hat{D}_2 - \alpha_0 = -\frac{k^2}{Re} - \alpha_0 \rightarrow -\alpha_0 \quad (61)$$

$$\hat{D}_3 - \alpha = -\frac{k^2 + \beta^2}{Re} - \alpha \rightarrow -(\alpha + \beta^2/Re) \quad (62)$$

In addition, incompressibility of the mode-1 fields (54) gives

$$\frac{ik_x}{\beta} \hat{u}_1 + \frac{ik_z}{\beta} \hat{w}_1 = \hat{v}_1. \quad (63)$$

Assuming eigenvector components \hat{u}_1 and \hat{w}_1 are $O(1)$, we have $\hat{v}_1 = O(\epsilon)$. Thus, terms involving k_x^2 , $k_x k_z$, $k_z \hat{v}_1$, and $k_z \hat{w}_1$ are $O(\epsilon^2)$. These term are shown in red in (59a)-(59f). Neglecting these terms, the eigenvalue equations become:

$$\sigma \hat{u}_0 + \frac{1}{2} ik_x u_{ss} \hat{u}_1 + \frac{1}{2} \beta u_{ss} \hat{v}_1 = \frac{k_x^2 \beta u_{ss}}{k^2} \hat{v}_1 - \alpha_0 \hat{u}_0 \quad (64a)$$

$$\sigma \hat{u}_1 + ik_x u_{ss} \hat{u}_0 = -(\alpha + \beta^2/Re) \hat{u}_1 - \beta \delta A_{ss} \hat{q}_0 \quad (64b)$$

$$\sigma \hat{v}_1 = -(\alpha + \beta^2/Re) \hat{v}_1 - ik_x \delta A_{ss} \hat{q}_0 \quad (64c)$$

$$\sigma \hat{w}_0 + \frac{1}{2} ik_x u_{ss} \hat{w}_1 = \frac{k_x k_z \beta u_{ss}}{k^2} \hat{v}_1 - \alpha_0 \hat{w}_0 \quad (64d)$$

$$\sigma \hat{w}_1 + ik_x u_{ss} \hat{w}_0 = -(\alpha + \beta^2/Re) \hat{w}_1 \quad (64e)$$

$$\sigma \hat{q}_0 = \frac{1}{2} A_{ss} \beta \hat{u}_1 + \hat{L} \hat{q}_0 \quad (64f)$$

This relatively simple eigenvalue problem captures well the onset of instability of the uniform turbulent fixed points (u_{ss}, q_{ss}) . Table I shows a comparison of eigenvalues for the full and simplified systems for relevant parameters.

full	-0.05972	$-0.03587 \pm 0.04809i$	$-0.02906 \pm 0.07571i$	0.00069
simplified	-0.05889	$-0.03505 \pm 0.04809i$	$-0.02841 \pm 0.07597i$	0.00104

TABLE I. Eigenvalues for the full eigenvalue problem (59) and simplified eigenvalue problem (64) for $Re = 82$, $k_x = 0.1$, $k_z = 0.24$.

B. Critical angle at onset of instability

The analysis can continue by focusing on the case of marginal stability, where $\sigma = 0$. No further simplifying assumptions are made and all calculations below follow exactly from eigenvalue problem (64). Setting $\sigma = 0$, equations (64) become algebraic equations

$$0 = \frac{1}{2}ik_x u_{ss} \hat{u}_1 + \beta u_{ss} \left(\frac{1}{2} - \frac{k_x^2}{k^2} \right) \hat{v}_1 + \alpha_0 \hat{u}_0 \quad (65a)$$

$$0 = ik_x u_{ss} \hat{u}_0 + (\alpha + \beta^2/Re) \hat{u}_1 + \beta \delta A_{ss} \hat{q}_0 \quad (65b)$$

$$0 = (\alpha + \beta^2/Re) \hat{v}_1 + ik_x \delta A_{ss} \hat{q}_0 \quad (65c)$$

$$0 = \frac{1}{2} \beta A_{ss} \hat{u}_1 + \hat{L} \hat{q}_0 \quad (65d)$$

We only need to consider these four equations, and not six, because \hat{w}_0 and \hat{w}_1 do not appear in these equations. We are not interested here in the critical eigenvector, but only in the parameter relations implied by a zero eigenvalue. This information is contained in (65).

Following straightforward elimination and back substitution, (65) reduces to:

$$\left\{ \frac{k_x^2 u_{ss}^2}{(\alpha + \beta^2/Re)} \left(\frac{1}{2} - \frac{k_x^2}{k^2} \right) + \left(\frac{1}{2} \frac{k_x^2 u_{ss}^2}{(\alpha + \beta^2/Re)} + \alpha_0 \right) \frac{2(\alpha + \beta^2/Re) \hat{L}}{\beta^2 A_{ss} \delta A_{ss}} - \alpha_0 \right\} \hat{q}_0 = 0. \quad (66)$$

The size of eigenvector component q_0 is arbitrary, hence the expression in brackets must vanish whenever there is a zero eigenvalue.

Expressions can be made more compact by introducing the following functions of Re

$$c_1(Re) = \frac{u_{ss}^2}{(\alpha + \beta^2/Re)} > 0, \quad c_2(Re) = \frac{2(\alpha + \beta^2/Re)}{\beta^2 A_{ss} \delta A_{ss}} > 0 \quad (67)$$

Note that since (u_{ss}, q_{ss}) depend on Re , so do A_{ss} and δA_{ss} . We emphasize that both are positive functions.

Rather than parameterizing eigenmodes modes by wavenumber pairs (k_x, k_z) , it is more useful to parameterize modes by (k, θ) , where

$$\tan \theta = \frac{k_x}{k_z}, \quad k^2 = k_x^2 + k_z^2 \quad (68)$$

The striped pattern with wavenumbers (k_x, k_z) makes angle θ with the streamwise direction. Using all the above, the condition for a zero eigenvalue becomes

$$c_1(Re) k^2 \sin^2 \theta \left(\frac{1}{2} - \sin^2 \theta \right) + \left(\frac{c_1(Re)}{2} k^2 \sin^2 \theta + \alpha_0 \right) c_2(Re) \hat{L}(k, \theta, Re) - \alpha_0 = 0 \quad (69)$$

We have explicitly indicated here that \hat{L} is a function of (k, θ, Re) . It is obtained from (45) by replacing $(\partial_x, \partial_z) \rightarrow (ik_x, ik_z)$ to give

$$\hat{L}(k, \theta, Re) = \frac{1}{2}\beta u_{ss} \delta A_{ss} - 2\alpha - \delta \varepsilon_{ss} - k^2 \left(\frac{1}{Re} + \nu_T(q_{ss}; Re) + c_3(Re) \sin^2 \theta \right), \quad (70)$$

where

$$c_3(Re) = \frac{u_{ss}^2}{2(2\alpha + 2\kappa + \beta^2/Re)} > 0, \quad (71)$$

is a third positive function of Re .

Letting $F_{\sigma=0}(k, \theta, Re)$ denote the left-hand side of (69), the condition for a zero eigenvalue, $\sigma = 0$, is written

$$F_{\sigma=0}(k, \theta, Re) = 0. \quad (72)$$

We are interested in the critical condition where a zero eigenvalue first appears with decreasing Re . This will demarcate the onset of turbulent bands. At such a point we must have

$$F_{\sigma=0}(k_c, \theta_c, Re_c) = 0, \quad (73a)$$

$$\left. \frac{\partial}{\partial k} F_{\sigma=0} \right|_{(k_c, \theta_c, Re_c)} = 0, \quad (73b)$$

$$\left. \frac{\partial}{\partial \theta} F_{\sigma=0} \right|_{(k_c, \theta_c, Re_c)} = 0, \quad (73c)$$

where Re_c is the critical Reynolds number at which instability first occurs, and (k_c, θ_c) are the associated critical wavenumber and critical angle.

(To understand why (73c) must hold, fix $k = k_c$ and suppose for that $\partial_\theta F_{\sigma=0} \neq 0$ at the critical point (k_c, θ_c, Re_c) . Then by the implicit function theorem, there is a function $\theta = g(Re)$ such that $F_{\sigma=0}(k_c, g(Re), Re) = 0$ for Re on an open interval containing Re_c . This implies that there is a zero eigenvalue both above and below Re_c . The contradicts the assumption that Re_c is the first value with decreasing Re for which there is a zero eigenvalue. A similar argument applies fixing θ and varying k .)

In principle, given the model closure parameters, equations (73) could be evaluated and used to find the critical point for the onset of bands. We will not pursue this here. However, we do consider just the condition on the angle (73c). Straightforward algebra gives

$$\sin^2 \theta_c = \frac{1}{4 + k^2 c_3(Re)} \left(1 + c_2(Re_c) \hat{L}(k_c, \theta_c, Re_c) - k^2 \frac{\alpha_0 c_3(Re)}{c_1(Re)} \right) \quad (74)$$

To get a bound on the critical angle θ_c , let \hat{L}_0 denote the terms in \hat{L} that are independent of wavenumber:

$$\hat{L}_0(Re) = \frac{1}{2}\beta u_{ss}\delta A_{ss} - 2\alpha - \delta\varepsilon_{ss} \quad (75)$$

All the other term in \hat{L} contain a factor $-k^2$. Hence, $\hat{L} < \hat{L}_0$. (In fact, the only positive term in \hat{L} is $\frac{1}{2}\beta u_{ss}\delta A_{ss}$.) Thus,

$$\sin^2 \theta_c \leq \frac{1}{4} \left(1 + c_2(Re_c)\hat{L}_0(Re_c) \right) \quad (76)$$

Consider now the system's homogeneous dynamics – the dynamics of spatially uniform states. In the absence of spatial dependence, we let $u_1(x, z, t) \rightarrow u(t)$ and $q_0(x, z, t) \rightarrow q(t)$. The (u, q) -dynamics are governed by the ODEs

$$\dot{u} = (\alpha + \beta^2/Re)(1 - u) - \beta A(q), \quad (77a)$$

$$\dot{q} = \frac{1}{2}\beta u A(q) - 2\alpha q - \varepsilon_0(q). \quad (77b)$$

Setting $\dot{u}_1 = \dot{q}_0 = 0$ gives the steady state equations (29), whose non-laminar solution is the uniform turbulent fixed point (u_{ss}, q_{ss}) . The stability of this state to uniform perturbation is determined by the linearization of (77). For (u_{ss}, q_{ss}) to be a linearly stable steady state of (77), the determinant of the 2×2 stability matrix must be positive. This gives

$$-(\alpha + \beta^2/Re) \left(\frac{1}{2}\beta u_{ss}\delta A_{ss} - 2\alpha - \delta\varepsilon_{ss} \right) + \frac{1}{2}\beta^2 A_{ss}\delta A_{ss} > 0 \quad (78)$$

or

$$\frac{2(\alpha + \beta^2/Re)\hat{L}_0}{\beta^2 A_{ss}\delta A_{ss}} = c_2(Re)\hat{L}_0(Re) < 1 \quad (79)$$

Using this bound in (76) gives

$$\sin^2 \theta_c < \frac{1}{2} \quad (80)$$

Hence, stability of the uniform turbulent state to uniform perturbations implies that the critical angle for turbulent bands at onset is less than 45° . While this is a statement about the onset of bands in the model, the result is independent of the particular form of the closures used and hence is a very general result. It is possible to improve the bound (80) by exploiting the specific closures used in the model, but we leave this for a future publication.

VI. DESCRIPTION OF SUPPLEMENTAL MOVIES

1. `Lx224Lz100_Re75_localized_initial.mp4`. Model run at $Re = 75$ from the localized initial condition (IC), with $(L_x, L_z) = (224, 100)$. Demonstrates growth from tips of band. Corresponds to panel (a) in Figure 2 of the main text.
2. `Lx224Lz100_Re75_localized.mp4`. Model run at $Re = 75$ from localized IC. Demonstrates evolution to steady band. Corresponds to panel (a) in Figure 2 of the main text.
3. `Lx224Lz100_Re78_localized_initial.mp4`. Model run at $Re = 78$ from localized IC, with $(L_x, L_z) = (224, 100)$. Demonstrates splitting mechanism. Corresponds to panel (b) in Figure 2 of the main text.
4. `Lx224Lz100_Re78_localized.mp4`. Model run at $Re = 78$ from localized IC. Demonstrates evolution to steady bands. Corresponds to panel (b) in Figure 2 of the main text.
5. `Lx224Lz100_Re78_uniform.mp4`. Model run at $Re = 78$ from the uniform turbulent fixed point IC $((u_{ss}, q_{ss})$ at $Re = 78$), with $(L_x, L_z) = (224, 100)$. Demonstrates breakdown of uniform turbulence at $Re < 85.1$. Corresponds to panel (c) in Figure 2 of the main text.
6. `Lx224Lz100_Re80_localized.mp4`. Model run at $Re = 80$ from localized IC, with $(L_x, L_z) = (224, 100)$. Demonstrates complex steady state – “criss-cross” pattern.
7. `Lx224Lz100_Re88_localized.mp4`. Model run at $Re = 88$ from localized IC, with $(L_x, L_z) = (224, 100)$. Demonstrates evolution to uniform turbulence beyond $Re = 85.1$.
8. `Lx224Lz200_Re75_localized_gauss.mp4`. Model run at $Re = 75$ from gaussian IC, with $(L_x, L_z) = (224, 200)$. Demonstrates the robustness of the band angle, even with different domain aspect ratios.
- 9.-11. `Lx448Lz200_Re{75,78,80}_localized.mp4`. Models run at $Re = 75, 78, 80$ from localized IC, with $(L_x, L_z) = (448, 200)$. The larger domain runs demonstrate the complexity of the transients (including different domains with opposite band angles), as

well as the variety of final banded states that can occur. `Lx448Lz200_Re80_localized.mp4` corresponds to Figure 2(e) from the main text.

- [1] F. Waleffe, On a self-sustaining process in shear flows, *Phys. Fluids* **9**, 883 (1997).
- [2] M. Chantry, L. S. Tuckerman, and D. Barkley, Turbulent-laminar patterns in shear flows without walls, *J. Fluid Mech.* **791**, R8 (2016).
- [3] L. S. Tuckerman, M. Chantry, and D. Barkley, Patterns in wall-bounded shear flows, *Annu. Rev. Fluid Mech.* **52**, 343 (2020).
- [4] B. Suri, J. Tithof, J. Mitchell, Radford, R. O. Grigoriev, and M. F. Schatz, Velocity profile in a two-layer Kolmogorov-like flow, *Phys. Fluids* **26**, 053601 (2014).
- [5] K. J. Burns, G. M. Vasil, J. S. Oishi, D. Lecoanet, and B. P. Brown, Dedalus: A flexible framework for numerical simulations with spectral methods, *Phys. Rev. Res.* **2**, 023068 (2020).
- [6] S. B. Pope, *Turbulent flows* (Cambridge university press, 2000).
- [7] D. Barkley, Modeling the transition to turbulence in shear flows, *Journal of Physics: Conference Series* **318**, 032001 (2011).
- [8] D. Barkley and L. S. Tuckerman, Computational study of turbulent-laminar patterns in Couette flow, *Phys. Rev. Lett.* **94**, 014502 (2005).